Regulation of coronavirus nsp15 cleavage specificity by RNA structure

Indranil Salukhe[1], Ryan Choi[2], Wesley Van Voorhis[2], Lynn Barrett[2], Jennifer L. Hyde[1]*

[1]Department of Microbiology, University of Washington School of Medicine, Seattle, WA, United States of America

[2]Division of Allergy and Infectious Diseases, Department of Medicine, Center for Emerging and Reemerging Infectious Diseases (CERID), University of Washington School of Medicine, Seattle, WA, United States of America

*Corresponding author: Jennifer L. Hyde, PhD, Department of Microbiology, University of Washington School of Medicine, Seattle WA 98109 USA Tel: 206-543-2820, Email: jlhyde4@uw.edu

Figures 3

Abstract

SARS-CoV-2, the etiologic agent of the COVID-19 pandemic, has had an enduring impact on global public health. However, SARS-CoV-2 is only one of multiple pathogenic human coronaviruses (CoVs) to have emerged since the turn of the century. CoVs encode for several nonstructural proteins (NSPS) that are essential for viral replication and pathogenesis. Among them is nsp15, a uridine-specific viral endonuclease that is important in evading the host immune response and promoting viral replication. Despite the established function of nsp15 as a uridine-specific endonuclease, little is known about other determinants of its cleavage specificity. In this study we investigate the role of RNA secondary structure in SARS-CoV-2 nsp15 endonuclease activity.

Using a series of *in vitro* endonuclease assays, we observed that thermodynamically stable RNA structures were protected from nsp15 cleavage relative to RNAs lacking stable structure. We leveraged the s2m RNA from the SARS 3'UTR as a model for our structural studies as it adopts a well-defined structure with several uridines, two of which are unpaired and thus high probably targets for nsp15 cleavage. We found that SARS-CoV-2 nsp15 specifically cleaves s2m at the unpaired uridine within the GNRNA pentaloop of the RNA. Further investigation revealed that the position of uridine within the pentaloop also impacted nsp15 cleavage efficiency, suggesting that positioning within the pentaloop is necessary for optimal presentation of the scissile uridine and alignment within the nsp15 catalytic pocket. Our findings indicate that RNA secondary structure is an important determinant of nsp15 cleavage and provides insight into the molecular mechanisms of recognition of RNA by nsp15.

Introduction

Coronaviruses (CoVs) are a diverse group of enveloped, positive sense single-stranded RNA (+ssRNA) viruses within the *Nidovirales* order which infect a wide range of host species and are associated with mild to severe disease in livestock and humans (1-3). The *Coronaviridae* family is composed of four genera: Alpha-, Beta-, Gamma-, and Deltacoronaviruses (4). Since the turn of the century, several pathogenic CoVs have emerged in the human population including SARS, MERS, and SARS-CoV-2 with the latter being the causative agent of the ongoing COVID-19 pandemic (1, 2).

Replication of the large (~30kb) CoV genome is facilitated by multiple nonstructural proteins (nsp1-16) which are produced from two open reading frames encoded by the first two thirds of the viral genome. These proteins encode several key functions necessary for synthesis and post-translational processing of the viral genome, including RNA-dependent RNA polymerase (nsp12), helicase (nsp13), RNA M7 and 2'-O-methyltransferase (nsp14, nsp16/nsp10), protease (nsp3, nsp5), and exonuclease (nsp14) activities. Structural proteins which assemble to form the virion, as well as accessory proteins, are encoded in a set of nested subgenomic RNAs which are coterminal with the 3' end of the genome.

The viral replication/transcription complex (RTC) is housed within membrane structures derived from the host endoplasmic reticulum (ER) which are induced by expression of nsp3, 4, and 6 (5-12). Like other +ssRNA viruses, these double-membrane vesicles (DMVs) provide a microenvironment that supports efficient viral replication and sequester double-stranded RNA (dsRNA) replication intermediates from detection by host pathogen recognition receptors (PRRs) (13, 14). Previous studies have demonstrated a key role for the interferon (IFN) response in restriction of CoVs. Accordingly, CoVs have evolved several mechanisms to evade antiviral immunity (e.g., 2'-O-methylation) and encode several proteins which antagonize the IFN response (nsp1, ORF6) (15). Nsp15 is a uridine-specific endonuclease (endoU) encoded by CoVs and other Nidoviruses which has been implicated in evasion of host-mediated RNA sensing and IFN activation (16, 17). While nsp15 has been shown to be non-essential for viral replication of several CoVs, absence of nsp15 endoU activity (Δnsp15) leads to greater accumulation of dsRNA replication intermediates which trigger IFN activation in immune competent cells such as macrophages (16). During CoV infection, dsRNA sensing occurs primarily via MDA-5, though other RNA sensors (PKR) have also been implicated (16, 18).

While originally described as a uridine-specific endonuclease, nsp15 has been shown to preferentially cleave pyrimidine-adenine dinucleotides ($U^{\downarrow}A$ or $C^{\downarrow}A$) (19). More recently, viral targets of nsp15 have been identified in both the polyU tract of tract of 5' negative-sense RNA,

as well as at several sites throughout the CoV genome (17, 19). Although multiple nsp15 cleavage sites have been mapped throughout the viral genome, no other sequence determinants have yet been identified. Despite the abundance of pyrimidine-adenine dinucleotides across the SARS-CoV-2 genome, only a fraction of these sites are cleaved by nsp15, suggesting that other RNA determinants likely affect cleavage specificity of viral RNA. Earlier *in vitro* studies have shown that SARS nsp15 cleaves a single unpaired uridine in the stem-loop II motif (s2m) RNA structural element found in the 3'-UTR of the viral genome suggesting that the structural context in which the scissile uridine is presented may play a role in determining nsp15 cleavage specificity (20). In this study, we use SARS s2m as a model RNA to explore the secondary structure requirements for SARS-CoV-2 nsp15 cleavage. Our findings reveal that thermodynamically stable RNAs are protected from SARS-CoV-2 nsp15 cleavage and cleaved less efficiently. We show for the first time that SARS-CoV-2 nsp15 preferentially cleaves unpaired bases. and show that the positioning and sequence context of the scissile uridine play a role in determining SARS-CoV-2 nsp15 cleavage specificity. This is consistent with previous studies of SARS nsp15, suggesting that SARS-CoV-2, and CoVs more broadly, may use RNA structure to regulate nsp15 cleavage specificity. These data shed further light on requirements for viral endoU target recognition and demonstrate an underappreciated role for viral RNA structure in evasion of innate immunity.

Results

RNA secondary structure modulates nsp15 cleavage efficiency

Nsp15 cleavage sites have previously been mapped in the MHV genome following viral infection (17, 19). Despite the abundance of pyrimidine-adenine dinucleotides throughout the genome, MHV nsp15 was found to cleave only a fraction of these sites, suggesting that other determinants play a role in CoV nsp15 cleavage specificity. We analyzed sequences upstream and downstream of MHV nsp15 cleavage sites to identify shared motifs that might contribute to nsp15 recognition and specificity. We reasoned that putative nsp15 recognition motifs present in the genome of MHV may also be conserved across other betacoronaviruses, including SARS-CoV-2. Using the MEME-suite XSTREME motif analysis and discovery tool (21) we analyzed 200 nt sequences corresponding to 100 nt upstream and downstream of the MHV nsp15 cleavage sites identified by Ancar et al. Although some motifs were found to be enriched in sequences surrounding the MHV nsp15 cleavage sites, they were not uniformly conserved across all cleavage sites. Moreover, many of these motifs were found at other sites in the viral

108 genome which were not previously identified as nsp15 targets and were not found to be
109 conserved in SARS-CoV-2 or other human CoVs.
110 As RNA structure has previously been implicated in nsp15 cleavage specificity (20), we
111 next compared the underlying predicted secondary structure of the same 200 nt fragments
112 using LocRNA software (22, 23). We did not identify any conserved structural elements at
113 nsp15 cleavage sites in MHV nor did we identify conserved structural elements upstream or
114 downstream of these sites. Despite the absence of any conserved sequence or structural
115 motifs, we hypothesized that the presence of thermodynamically stable RNA elements would
116 prevent cleavage of RNA by nsp15.
117 To test this hypothesis, we used RNAfold (24) to identify regions across the SARS-CoV-
118 2 genome predicted to have varying degrees of thermodynamic stability (Fig. 1A; RNA 1, RNA
119 2, RNA 3) (25, 26). We identified representative regions of high, moderate, and low
120 thermodynamic stability as indicated by their relative ΔG values (Fig. 1B), with more stable
121 predicted structures having lower ΔG values (27). 100 nt RNAs corresponding to these regions
122 were synthesized *in vitro*, and cleavage efficiency of these RNAs was assessed using a SARS-
123 CoV-2 nsp15 endonuclease assay (28) (Fig. 1C and D). Folded RNAs were incubated with
124 recombinant SARS-CoV-2 nsp15 for varying times (1, 15, 60, and 240 minutes) and cleavage
125 products analyzed by polyacrylamide gel electrophoresis (Fig. 1C). Cleavage of full-length RNA
126 was additionally quantified by densitometry by comparing the abundance of full-length RNA at
127 each time point to a denatured nsp15 control (no cleavage, (-) far-right lane) (Fig. 1D). As we
128 hypothesized, we observed that RNAs with relatively moderate or low predicted thermodynamic
129 stability were cleaved more rapidly than RNA with relatively high thermodynamically stability
130 (Fig. 1C, compare abundance of full-length transcript at 1, 15 and 60 min [red arrow]; Fig. 1D
131 compare percentage uncleaved RNA). Notably, RNA with relatively low thermodynamic stability
132 showed rapid cleavage as early as 1 min following the addition of nsp15. While each RNA
133 yielded different cleavage products owing to the differences in RNA sequence, we observed the
134 appearance of distinct cleavage products that either decreased (green arrows) or increased
135 (blue arrows) in abundance over time. These likely represent cleavage intermediates or end
136 products respectively, suggesting that other structural features or specific sequences also likely
137 contribute to the higher efficiency of nsp15 cleavage of some RNA sequences over others.
138 Collectively, these data suggest that RNA secondary structure impacts nsp15-dependent RNA
139 cleavage.
140
141 **SARS-CoV-2 nsp15 cleaves unpaired bases in structured RNAs**

142 In vitro biochemical studies by Bhardwaj et al. previously showed that SARS nsp15
143 specifically cleaves 3' of unpaired uridines in s2m, a conserved structural element found in the
144 3'UTR of the SARS genome and some other related CoVs (20, 29, 30). In addition to our results
145 described above (Fig. 1), this study suggests that the context in which the cleaved uridine is
146 presented may be important for determining the cleavage specificity of nsp15. In the case of
147 s2m, the two unpaired uridines (U25 and U30) are located in two unstructured loops (Fig. 2A,
148 highlighted in blue). Structural resolution of s2m has shown that U25, which is located within the
149 GNRNA sequence of the pentaloop of s2m, is highly disordered relative to other nucleotides,
150 and that U30 is also moderately disordered (29). Based on previous findings and the availability
151 of structural information, we posited that s2m would be a tractable model RNA for studying the
152 determinants of cleavage specificity of SARS-CoV-2 nsp15.
153 We first sought to determine whether SARS-CoV-2 nsp15 exhibits cleavage specificity
154 for unpaired uridines in s2m similar to that previously observed for SARS nsp15 (20). To identify
155 whether nsp15 preferentially cleaves at U25, U30, or both, we generated wild type (wt) SARS
156 s2m RNA, as well as single and double s2m mutants containing U-to-A substitutions at U25 and
157 U30 (Fig. 2A) and compared cleavage efficiency of these RNAs via endonuclease assay (Fig.
158 2A and B). In contrast to wt s2m, cleavage of the double mutant ($s2m_{mut3}$) was noticeably
159 impaired, consistent with previous studies showing nsp15 cleavage preference for unpaired
160 uridines. However, in contrast to previous findings with SARS nsp15, we observed that mutation
161 of U30 (U30A; $s2m_{mut2}$) did not impact RNA cleavage, whereas mutation of U25 (U25A; $s2m_{mut1}$)
162 did. Although quantitative differences in full-length RNA cleavage were not found to be
163 statistically significant (Fig 2B), accumulation of cleavage products in the U25A ($s2m_{mut1}$) and
164 double mutant ($s2m_{mut3}$) was clearly impaired relative to wt and U30A ($s2m_{mut2}$) RNAs.
165 Interestingly, we also observed accumulation of distinct cleavage products in $s2m_{mut1}$ and
166 $s2m_{mut3}$. This may indicate that step wise cleavage of RNA and RNA intermediates is altered in
167 the absence of the scissile U25. However, while mutation of U25 was not predicted to impact
168 the structure of s2m using RNAfold analysis (Fig. 2C), we cannot rule out the possibility that
169 mutation of U25 leads to changes in s2m RNA structure which impact nsp15-mediated
170 cleavage.
171 Due to the presence of multiple uridines in s2m, accurate identification of cleavage
172 products and intermediates was challenging. In order to eliminate extraneous cleavage products
173 to clarify interpretation of endonuclease data and further dissect RNA structural determinants of
174 cleavage efficiency, we designed truncated s2m RNAs (Δs2m) which lack the base of the stem
175 and all uridines except U25 and U30 (Fig. 2D). Similar to the experiments described above, we

176 also engineered Δs2m mutants with U-to-A substitutions at U13 ($\Delta s2m_{mut1}$) and U18 ($\Delta s2m_{mut2}$)
177 (equivalent to U25 and U30 in wt s2m), or both U13 and U18 ($\Delta s2m_{mut3}$). As with the full-length
178 s2m RNAs, the free energies and ensemble diversities of the ∆s2m mutant RNAs were similar
179 to each other (Fig. 2C). We analyzed cleavage of wt and mutant Δs2m RNAs over time by
180 endonuclease assay as described above (Fig 2D and E). In keeping with experiments with full-
181 length s2m RNA, we observed rapid accumulation of cleavage products in wt Δs2m and
182 $\Delta s2m_{mut2}$ RNAs. In contrast, mutation of both U13 and U18 (U25 and U30 equivalent), or U13
183 (U25 equivalent) alone, resulted in delayed and reduced nsp15 cleavage of RNA. Interestingly,
184 we still observed some modest cleavage of $\Delta s2m_{mut1}$ suggesting that while U13 is the
185 predominant cleavage site in the Δs2m RNA, nsp15 is also able to recognize and cleave at
186 other sites. While mutation of both U13 and U18 led to a further reduction in nsp15-mediated
187 cleavage, some cleavage products were still detected in the double mutant, lending further
188 support to the hypothesis that nsp15 can also cleave non-uridine bases, albeit at lower
189 efficiency. Indeed, while nsp15 displays a strong preference of cleavage 3' of uridines, previous
190 work has shown that cleavage at other bases (especially cytosine) also occurs (31).
191 We hypothesized that RNA secondary structure contributes to nsp15 cleavage specificity
192 by presenting the scissile uridine in a structural context favorable for nsp15 cleavage. However,
193 an alternative explanation could be that RNA structure serves to sterically hinder or promote
194 nsp15-RNA binding. To address whether differences we observed in cleavage of wt and mutant
195 Δs2m RNAs was due to differences in protein-RNA binding alone, we compared nsp15-RNA
196 binding affinities using differential radial capillary of action ligand assay (DRaCALA) (32, 33).
197 Here, 5'-end radiolabeled Δs2m RNAs were incubated with increasing concentrations of
198 recombinant mutant nsp15 (nsp15 (K290A)), complexes applied to nitrocellulose membrane,
199 and the fraction of bound vs unbound RNA quantified (Fig. 2F). Nsp15 (K290A) was used to
200 eliminate endonuclease activity and contains a mutation of one of the conserved catalytic
201 residues necessary for endoU activity (20, 34-36). We compared binding of wt and mutant
202 Δs2m RNA, in addition to full-length wt s2m. The latter was chosen as a control, as it is
203 presently unknown what the minimum length requirement is for RNA recognition and binding by
204 nsp15. We observed binding of nsp15 (K290A) to wt Δs2m (K_D=1.5μM). When we compared
205 binding of K290A to each mutant Δs2m RNA, we observed only slight decreases in binding
206 affinity (approximately 1.3-fold; $\Delta s2m_{mut1}$ K_D=2.0μM, $\Delta s2m_{mut2}$ K_D=1.9μM, $\Delta s2m_{mut3}$ K_D=8.5μM),
207 which were not found to be statistically significant. Notably, we observed a modest increase in
208 binding affinity of K290A for the full-length s2m RNA (approximately 4-fold; s2m K_D=0.3μM)
209 suggesting that other RNA-protein contacts in longer RNAs may modestly contribute to binding

210 affinity. As nsp15 exhibited similar binding affinities for all Δs2m RNAs we concluded that
211 differences in cleavage efficiency of Δs2m RNAs is not due to differences in protein-RNA
212 binding, but likely driven by positioning of the scissile uridine in these differently structured
213 RNAs.
214
215 **Flexible uridine nucleotides in structured pentaloops are susceptible to SARS-CoV-2**
216 **nsp15 cleavage**
217 Recent structural studies have suggested that SARS-CoV-2 nsp15 uses a base flipping
218 mechanism to position the scissile uridine in the catalytic pocket, thus enabling cleavage of
219 dsRNA (37). The crystal structure of s2m shows that U25 in the GNRNA pentaloop adopts a
220 similar flipped out orientation (29) suggesting that this mechanism could also account for the
221 specificity of nsp15 cleavage for U25 in s2m. RNA pentaloops adopt a characteristic structure
222 which consists of a sheared G-A base pair that closes the pentaloop and induces base stacking
223 of first N, R, and A nucleotides. Notably, this conformation induces extrusion (or 'flipping') of the
224 second N (GNR**N**A) in the pentaloop (38, 39). Thus, we postulated that the position of the
225 scissile uridine in the pentaloop (GAG**U**A) might be necessary to confer the correct orientation
226 required for nsp15 cleavage. To test whether the relative position of U25 is necessary for
227 cleavage specificity, we constructed two additional Δs2m mutants in which the position of
228 scissile uridine has been altered (Fig. 3A, top), and compared cleavage efficiency in the endoU
229 assay (Fig 3A, bottom). In $\Delta s2m_{mut4}$ the adjacent guanidine and uridine in the pentaloop were
230 swapped (GA**UG**A), such that the scissile uridine now sits at the apex of the pentaloop. In
231 $\Delta s2m_{mut5}$ the scissile uridine was positioned downstream at the 3' end of the pentaloop and
232 adjacent to closing GC base pair of the helix (GAGA**U**). The second uridine in the bulge of
233 Δs2m (U18) was also mutated in both RNAs in order to assess the impact of U13 (U25
234 equivalent in full-length s2m) cleavage only. We predicted that in $\Delta s2m_{mut4}$ positioning of the
235 scissile uridine at the apex would have minimal effect on cleavage but that placement of uridine
236 adjacent to the helix would place structural constraints on this base such that it would be unable
237 to adopt the necessary conformation (flipped out) required for positioning within the catalytic
238 pocket of nsp15. When we compared cleavage of each mutant, we observed that $\Delta s2m_{mut4}$
239 (GA**U**GA) was cleaved to completion earlier than both $\Delta s2m_{mut2}$ (control) and $\Delta s2m_{mut5}$
240 (GAGA**U**) (Figure 3B). In contrast, we observed almost no cleavage of $\Delta s2m_{mut5}$ supporting the
241 hypothesis that the scissile uridine might be more structurally constrained at this position and
242 unable to engage with the catalytic pocket of nsp15. From these data, we concluded that uridine

position within the pentaloop influences nsp15 cleavage activity, likely through structural constraints.

Discussion

Nsp15 is a viral endonuclease conserved across the *Nidovirales* and plays a crucial role in CoV evasion of host innate immunity. The crystal structure of several CoV nsp15 proteins has been solved to date, including SARS-CoV-2 (34, 36, 40-44). Structural and biochemical analyses have revealed key aspects of nsp15 function, including the requirement of Mn^{2+} for endonuclease activity at neutral pH as well as formation of higher order oligomers (hexamers) which is also necessary for endoU function (20, 34, 35, 40, 44, 45). Nsp15 primarily functions to evade innate immune responses by cleaving dsRNA replicative intermediates and preventing activation of MDA-5, and possibly other RNA sensors in the host cell (16-19, 46-50). Some studies also suggest that CoV nsp15 may play a role in viral transcriptional regulation during viral replication (19) and that endoU-independent activities additionally contribute to modulation of host responses (49, 51-54).

At present, the RNA targets of nsp15 endoU from across the *Coronaviridae* are poorly defined. This can be attributed in part to the fact that in vitro studies have used different RNA species (dsRNA vs ssRNA) and different RNA sequences and lengths, making cross-comparison of these data challenging. Nsp15 has been shown to cleave 3' of pyrimidines, in particular uridine, and exhibit a preference for weak bases (A or U) 3' of the scissile nucleotide. However, to date no specific nsp15 recognition motifs have been described. Indeed, our analysis of previously identified MHV nsp15 cleavage sites (19) failed to identify novel sequence motifs in and around the cleavage site (data not shown). In the absence of a sequence motif, we postulate that RNA secondary structure may function to regulate both RNA binding and cleavage efficiency of nsp15.

To this end, recent work has shown that SARS-CoV-2 nsp15 manipulates the scissile uridine for cleavage of dsRNA (37). However, the extent to which RNA secondary structure is involved in modulating SARS-CoV-2 nsp15 cleavage activity remains to be determined. Thus, in this study we sought to determine the role of RNA structure in the regulation of SARS-CoV-2 nsp15-mediated cleavage and define specific structural features of RNAs that contribute to this. We demonstrated that increased thermodynamic stability of RNA is associated with decreased nsp15 cleavage efficiency (Fig. 1) and postulated that stable secondary structure may contribute to nsp15 cleavage by two modes: 1) steric hinderance; and 2) inducing optimal positioning of

the scissile uridine in the nsp15-RNA complex. To test this second hypothesis, we used s2m as a model RNA to explore the RNA determinants of nsp15 cleavage specificity.

Using a genetic approach, we first demonstrated that nsp15 exhibits specificity for cleavage of the uridine nucleotide located in the GNRNA pentaloop of s2m (Fig. 2, Fig. 3). This contrasts with previous data from Bhardwaj et al., in which the authors observed preferential cleavage of U30, located in the bulge sequence downstream of the pentaloop (20). It should be noted that these previous studies were performed with SARS nsp15, which shares 88% identity with SARS-CoV-2 nsp15. One explanation for the discrepancy in our data could be structural differences between these proteins which lead to altered cleavage specificity.

Notably, the specificity for cleavage of the pentaloop uridine (GAG**U**A) was not due to differences in nsp15-RNA binding (Fig. 2F), thus we postulated that the sequence context of the scissile uridine might be important for this specificity. The characteristic structure adopted by GNRNA pentaloops induces extrusion, or base flipping, of the scissile uridine away from the body of the RNA (38, 39), and this base flipping mechanism has been suggested to be important for correct positioning of uridine in the catalytic pocket of nsp15 (55). Pentaloop motifs have also been implicated in base editing mediated by Adenosine Deaminases that Act on RNA 2 (ADAR2) (56), though in this instance the GCUMA pentaloop is located downstream of the edited A, and is implicated in recruitment of ADAR2 via interactions between the dsRNA binding motif of ADAR2 and the target RNA. We speculated that if structural conformation of the scissile uridine was important for base recognition and cleavage that altering the position (and conformation) of the uridine base would lead to altered cleavage efficiency. Indeed, repositioning of the scissile uridine to the apex of the pentaloop ($\Delta s2m_{mut4}$) slightly enhanced cleavage efficiency RNA, whereas repositioning adjacent to the closing G-C base pair ($\Delta s2m_{mut5}$) significantly reduced RNA cleavage (Fig. 3). The marked decrease in $\Delta s2m_{mut5}$ cleavage is likely due to altered positioning of the scissile uridine which we predict is no longer extruded from the pentaloop, as well as decreased flexibility of this base which is now structurally constrained by the neighboring G-C base pair. Another possibility is that cleavage efficiency is impacted by altering the sequence context of the scissile uridine. Nsp15 has been shown to preferentially cleave uridines flanked by a weak base (A/U) which is found in wt Δs2m and $\Delta s2m_{mut2}$ ($U^{\downarrow}A$) but is changed to a strong base in $\Delta s2m_{mut5}$ ($U^{\downarrow}C$). However, we observed a modest increase in cleavage efficiency of $\Delta s2m_{mut4}$ which also has a strong base at the 3' position ($U^{\downarrow}G$) and lends support to the hypothesis that the structural context of the scissile uridine, not sequence context, may be more relevant in dictating cleavage specificity and efficiency.

310 Collectively, our data suggests that RNA secondary structure plays two distinct roles in
311 determining nsp15 cleavage specificity. First, thermodynamically stable structures likely
312 sterically hinder nsp15-RNA interactions, thus preventing engagement and cleavage of some
313 RNA sequences. Second, susceptible bases are presented in a structural context which
314 facilitates optimal positioning of the scissile nucleotide in the catalytic pocket of nsp15 (e.g.,
315 extrusion of the scissile U25 in the GNRNA pentaloop). However, several questions remain
316 unanswered, most notably, what are the biologically relevant targets (host and viral) of nsp15
317 cleavage during CoV infection and are viral targets conserved across different CoVs? Two
318 studies to date have identified cleavage sites within the positive-sense genomic RNA and 3'
319 polyU tails of the negative-sense RNA of MHV (17, 19). Despite this, no recognition motif or
320 other regulatory element associated with nsp15 cleavage has been identified. While the in vitro
321 assays performed here and in other studies provide a tractable system for dissecting the
322 molecular mechanism of nsp15-RNA interactions and cleavage determinants, nsp15 forms part
323 of a larger replication-transcription complex (RTC) which contains other viral proteins and host
324 factors. How nsp15 protein-protein interactions and RNA interactions with other replicase
325 proteins (e.g., nsp12, nsp14, nsp16) impacts nsp15 cleavage of RNA still remains unsolved.
326 Indeed, recent models of the RTC suggest the hexameric structure of nsp15 provides the
327 central structure and arrangement of a hexameric RTC (57). When nsp15 is bound in the RTC
328 structure, there may be differences in its cleavage of viral RNAs due to its 3-D interaction with
329 the nascent RNA as opposed to when nsp15 is free from the RTC as was the case in this study.
330 The importance of examining nsp15-RNA interactions in their relevant biological context is
331 further highlighted by recent studies showing that the requirement for Mn^{2+} and the structural
332 conformation of nsp15 is highly dependent on the pH of the environment (58). Given that the
333 redox state of the viral RTC of +ssRNA viruses is altered during replication, the conditions under
334 which nsp15 endoU activity is examined is highly relevant. To address this our future studies will
335 explore the impact of pH and redox state on nsp15 structure and function in vitro.
336 Overall, our findings suggest a role for RNA secondary structure in regulation of nsp15
337 cleavage. Identification of bona fide nsp15 cleavage sites in SARS-CoV-2 RNA during
338 replication and examination of how perturbation of these sites impacts the outcome of
339 replication and pathogenesis will provide key insight into the broader roles for nsp15 endoU
340 activity during infection (e.g., viral transcriptional/translational regulation, host translation).
341 Furthermore, defining key structural features of RNAs which are resistant or susceptible to
342 nsp15 cleavage may provide avenues for development of antiviral therapeutics.
343

Acknowledgements

The authors declare that they have no conflict of interest.

Materials and Methods

Generation of SARS-CoV-2 RNA segments: 100nt segments of SARS-CoV-2 genome were amplified using the primers listed in Table 1. Amplicons were purified using Mag-Bind Total Pure NGS beads (Omega Bio-Tek). 1.5 x bead volume relative to amplification reactions was used and purified as per manufacturer's instructions. Purified amplicons were subcloned into a vector containing the HDV ribozyme (59). These constructs were linearized and purified prior to transcription.

Approximately 5 pmol of purified DNA was used as a template for T7 transcription reactions. RNAs were transcribed using the HiScribe T7 High Yield RNA Synthesis Kit (New England Biolabs). Reactions were set up as per manufacturer's instructions with the addition of 4 units of Murine RNase Inhibitor (NEB) and 5% DMSO. Transcriptions were incubated at 42°C overnight after which, the reactions were treated with DNaseI (NEB) as per manufacturer's instructions. DNase-treated transcriptions were then purified using Mag-Bind Total Pure NGS beads as described above.

Transcriptions were gel purified by running samples on urea gels. 15% TBE-Urea gels were made using SequaGel UreaGel 29:1 Denaturing Gel System (National Diagnostics) Urea was added to the samples to a final concentration of 4M before running on the gels at 200V for 90 minutes. Gels were briefly stained with 0.02% Methylene Blue in TBE until ladder was visible. Gels were imaged on Gel Doc XR+(Bio-Rad), and bands corresponding to 100nt fragments were cut out and shredded by centrifugation. RNAs were eluted overnight on rotator in 3x volume of elution buffer (10mM Tris-HCl, 1mM EDTA, 300mM NaCl, 0.1% SDS) relative to gel weight. Gel slurries were applied to cellulose acetate columns and frozen at -80°C for 10 minutes. Samples were centrifuged at 10,000x g for 3 minutes. Eluate was adjusted up to 600µL with nuclease-free water and purified by acid phenol-chloroform extraction.

Table 1

RNA	Forward Primer	Reverse Primer
RNA 1	CATGAGCTTA AGTAATACGA CTCACTATAG GCTACTAACA ATGCCAT	CATGAGGCTA GCAAGATTGT GTCCGCTTAA AA

RNA 2	CATGAGCTTA AGTAATACGA CTCACTATAG ACCTGAGCAT AGTCTTG	CATGAGGCTA GCGAGAACAC ACAGCCTC
RNA 3	CATGAGCTTA AGTAATACGA CTCACTATAG TGAAGTGCTG TCTGAC	CATGAGGCTA GCGTTACACG ATAACCAGTA AAG

374

375 *Endonuclease Assay:* Indicated amounts of RNAs were diluted in folding buffer (50mM
376 Tris-HCl, 50mM KCl, 5mM $MgCl_2$, 5mM DTT). RNAs were incubated at 95°C for 10 minutes
377 then cooled to 25°C at a rate of 0.1°C/sec. Purified nsp15 was diluted in assay buffer (50mM
378 Tris-HCl, 50mM KCl, 50mM $MnCl_2$, 5mM $MgCl_2$, 5mM DTT) to the appropriate concentration for
379 indicated nsp15:RNA ratios. Recombinant nsp15 was expressed and purified as previously
380 described (60). To denature nsp15, the protein was incubated at 95°C for 5 minutes. Folded
381 RNA was aliquoted into individual tubes (1 tube/timepoint), and diluted nsp15 was mixed in
382 equal amounts to each RNA simultaneously. Reactions were arrested at indicated timepoints
383 with a final concentration of 20mM EDTA before flash freezing in liquid nitrogen. Denatured
384 nsp15 reactions were incubated for 240 minutes.
385 TBE-Urea gels were made using SequaGel UreaGel 29:1 Denaturing Gel Syst
386 em (National Diagnostics). 15% or 22.5% gels were poured as indicated in each experiment.
387 RNA samples were thawed and mixed with an equal volume of 2x RNA Loading Dye (NEB) and
388 loaded onto the gels. Gels were run at 200V for 1 hour in 1x TBE. Gels were stained with SYBR
389 Green (ThermoFisher) diluted 1:5000 in TBE for 30 minutes while shaking and imaged on Gel
390 Doc XR+(Bio-Rad). Full-length bands for at each time point were calculated by densitometry
391 using Image Lab software (Bio-Rad). Density of bands were normalized to denatured nsp15
392 control for each reaction.
393

394 *DRaCALA:* DRaCALAs were performed as described previously (32). Briefly, RNAs
395 were dephosphorylated and 5' radiolabeled with 30μCi ATP. Radiolabeled RNAs were set up in
396 reactions with the following components: DRaCALA buffer (50mM HEPES, 100mM KCl), 5mM
397 $MgCl_2$, 50ng/μL yeast tRNA, 1mM DTT, 5% glycerol. RNAs were heated to 95°C for 2 minutes
398 and cooled at RT for 10 minutes. Serial dilutions of nsp15 K290A were added to the reactions
399 which were incubated for 15 minutes at RT and spotted onto a 0.45μm nitrocellulose
400 membrane. Blots were exposed to a phosphor screen overnight and imaged on Sapphire
401 Molecular Imager (Azure Biosystems). Binding was measured by densitometry as previously
402 described (33) using Fiji.
403

404 **FIGURE LEGENDS**

405 **Figure 1. Secondary structure protects RNA from cleavage by SARS-CoV-2 nsp15. A.**
406 Predicted minimum free energy structures (RNAfold) of 100 nt RNAs from the SARS-CoV-2
407 genome of varying thermodynamic stability (high, medium, and low). Unpaired uridines are
408 highlighted in blue, and paired uridines are outlined in blue. All RNA structures were predicted in
409 RNAfold and designed in RNA2Drawer (27, 61). **B.** The locations within the SARS-CoV-2
410 genome are indicated for each structure, and thermodynamic stability is indicated as -ΔG.
411 Ensemble diversity is listed as predicted by RNAfold. **C.** Endonuclease assays of RNAs from
412 (A). Full-length (uncut) RNAs are indicated by the red arrows. Diminishing cleavage products
413 (cleavage intermediates) are indicated by green arrows. Accumulating cleavage products
414 (cleavage end products) indicated by blue arrows. Representative images from one of three
415 total experiments are shown. **D.** Quantitation of data from (C). The percentage of full-length
416 RNA remaining was measured by densitometry. Most thermodynamically stable RNA (RNA 1)
417 was cleaved least rapidly relative to other RNAs. Percentage of uncut RNA was calculated by
418 normalizing to a denatured nsp15 control (indicated by (-) in the far-right lane). Area under the
419 curve (AUC) was calculated for each RNA and one-way ANOVA with multiple comparisons was
420 performed on the AUC. Data represents three independent experiments.

421

422 **Figure 2. SARS-CoV-2 nsp15 cleaves structured RNAs at specific sites. A.** Endonuclease
423 assays of full-length s2m mutant RNAs. Full-length bands indicated at the top of the gel with
424 cleavage products below. Representative images from one experiment. **B.** Percent of full-length
425 RNA remaining as measured by densitometry. Percentage of uncut RNA was calculated by
426 normalizing to a denatured nsp15 control (indicated by (-) in the far-right lane). RNAs with
427 uridines present in the pentaloop (s2m and $s2m_{mut2}$) cleaved more efficiently than $s2m_{mut}1$ and
428 $s2m_{mut3}$. AUC was calculated for each RNA and one-way ANOVA with multiple comparisons
429 was performed on the AUC. AUC of s2m mutant RNAs are compared to wt s2m. Data
430 represents three independent experiments. **C.** Thermodynamic stability and ensemble diversity
431 of s2m and mutant RNAs indicated as predicted by RNAfold. **D.** Endonuclease assays of
432 modified s2m RNAs. Full-length bands indicated at the top of the gel with cleavage products
433 below. Representative images from one experiment. **E.** Percent of full-length RNA remaining as
434 measured by densitometry. Percentage of uncut RNA was calculated by normalizing to a
435 denatured nsp15 control (indicated by (-) in the far-right lane). RNAs with uridines present in the
436 pentaloop (Δs2m and $\Delta s2m_{mut2}$) cleaved more efficiently than $\Delta s2m_{mut}1$ and $\Delta s2m_{mut3}$. AUC was
437 calculated for each RNA and one-way ANOVA with multiple comparisons was performed on the

438 AUC. AUC of ∆s2m mutant RNAs are compared to wt ∆s2m. Data represents three independent
439 experiments. **F.** Nsp15 binding curves of Δs2m RNAs as compared to wt s2m. ∆s2m RNA
440 binding curves overlap with each other while wt s2m curve is shifted left indicating improved
441 binding with nsp15. Dissociation constant (K_D) was calculated for each RNA and one-way
442 ANOVA with multiple comparisons was performed on the K_D. AUC of wt full-length s2m and
443 ∆s2m mutant RNAs are compared to wt ∆s2m. Data represents three independent experiments.
444
445 **Figure 3. Uracil position in loop structures impacts SARS-CoV-2 nsp15 cleavage**
446 **efficiency. A.** Endonuclease assays of s2m pentaloop mutant RNAs. Full-length bands
447 indicated at the top of the gel with cleavage products below. Representative images from one
448 experiment. **B.** Thermodynamic stability and ensemble diversity of s2m and mutant RNAs
449 indicated as predicted by RNAfold. **C.** Percent of full-length RNA remaining as measured by
450 densitometry. Percentage of uncut RNA was calculated by normalizing to a denatured nsp15
451 control (indicated by (-) in the far-right lane). RNAs with uridines positioned closer to the apex of
452 the pentaloop cleaved more rapidly than $\Delta s2m_{mut5}$ in which the uridine is at the end of the
453 pentaloop. AUC was calculated for each RNA and one-way ANOVA with multiple comparisons
454 was performed on the AUC. Data represents three independent experiments.
455
456 **References**

457 1. Zhou P, Yang XL, Wang XG, Hu B, Zhang L, Zhang W, et al. A pneumonia outbreak
458 associated with a new coronavirus of probable bat origin. Nature. 2020;579(7798):270-3.
459 2. Helmy YA, Fawzy M, Elaswad A, Sobieh A, Kenney SP, Shehata AA. The COVID-19
460 Pandemic: A Comprehensive Review of Taxonomy, Genetics, Epidemiology, Diagnosis,
461 Treatment, and Control. J Clin Med. 2020;9(4).
462 3. Weiss SR, Navas-Martin S. Coronavirus pathogenesis and the emerging pathogen severe
463 acute respiratory syndrome coronavirus. Microbiol Mol Biol Rev. 2005;69(4):635-64.
464 4. Luk HKH, Li X, Fung J, Lau SKP, Woo PCY. Molecular epidemiology, evolution and
465 phylogeny of SARS coronavirus. Infect Genet Evol. 2019;71:21-30.
466 5. Ricciardi S, Guarino AM, Giaquinto L, Polishchuk EV, Santoro M, Di Tullio G, et al. The
467 role of NSP6 in the biogenesis of the SARS-CoV-2 replication organelle. Nature.
468 2022;606(7915):761-8.
469 6. Oudshoorn D, Rijs K, Limpens R, Groen K, Koster AJ, Snijder EJ, et al. Expression and
470 Cleavage of Middle East Respiratory Syndrome Coronavirus nsp3-4 Polyprotein Induce the
471 Formation of Double-Membrane Vesicles That Mimic Those Associated with Coronaviral RNA
472 Replication. mBio. 2017;8(6).
473 7. Lundin A, Dijkman R, Bergstrom T, Kann N, Adamiak B, Hannoun C, et al. Targeting
474 membrane-bound viral RNA synthesis reveals potent inhibition of diverse coronaviruses
475 including the middle East respiratory syndrome virus. PLoS Pathog. 2014;10(5):e1004166.

476 8. Angelini MM, Akhlaghpour M, Neuman BW, Buchmeier MJ. Severe acute respiratory
477 syndrome coronavirus nonstructural proteins 3, 4, and 6 induce double-membrane vesicles.
478 mBio. 2013;4(4).
479 9. Gosert R, Kanjanahaluethai A, Egger D, Bienz K, Baker SC. RNA replication of mouse
480 hepatitis virus takes place at double-membrane vesicles. J Virol. 2002;76(8):3697-708.
481 10. van der Meer Y, Snijder EJ, Dobbe JC, Schleich S, Denison MR, Spaan WJ, et al.
482 Localization of mouse hepatitis virus nonstructural proteins and RNA synthesis indicates a role
483 for late endosomes in viral replication. J Virol. 1999;73(9):7641-57.
484 11. Shi ST, Schiller JJ, Kanjanahaluethai A, Baker SC, Oh JW, Lai MM. Colocalization and
485 membrane association of murine hepatitis virus gene 1 products and De novo-synthesized viral
486 RNA in infected cells. J Virol. 1999;73(7):5957-69.
487 12. Prentice E, Jerome WG, Yoshimori T, Mizushima N, Denison MR. Coronavirus replication
488 complex formation utilizes components of cellular autophagy. J Biol Chem.
489 2004;279(11):10136-41.
490 13. Overby AK, Popov VL, Niedrig M, Weber F. Tick-borne encephalitis virus delays
491 interferon induction and hides its double-stranded RNA in intracellular membrane vesicles. J
492 Virol. 2010;84(17):8470-83.
493 14. Knoops K, Kikkert M, Worm SH, Zevenhoven-Dobbe JC, van der Meer Y, Koster AJ, et al.
494 SARS-coronavirus replication is supported by a reticulovesicular network of modified
495 endoplasmic reticulum. PLoS biology. 2008;6(9):e226.
496 15. Kamitani W, Narayanan K, Huang C, Lokugamage K, Ikegami T, Ito N, et al. Severe acute
497 respiratory syndrome coronavirus nsp1 protein suppresses host gene expression by promoting
498 host mRNA degradation. Proc Natl Acad Sci U S A. 2006;103(34):12885-90.
499 16. Deng X, Hackbart M, Mettelman RC, O'Brien A, Mielech AM, Yi G, et al. Coronavirus
500 nonstructural protein 15 mediates evasion of dsRNA sensors and limits apoptosis in
501 macrophages. Proc Natl Acad Sci U S A. 2017;114(21):E4251-E60.
502 17. Hackbart M, Deng X, Baker SC. Coronavirus endoribonuclease targets viral polyuridine
503 sequences to evade activating host sensors. Proc Natl Acad Sci U S A. 2020;117(14):8094-103.
504 18. Kindler E, Gil-Cruz C, Spanier J, Li Y, Wilhelm J, Rabouw HH, et al. Early endonuclease-
505 mediated evasion of RNA sensing ensures efficient coronavirus replication. PLoS Pathog.
506 2017;13(2):e1006195.
507 19. Ancar R, Li Y, Kindler E, Cooper DA, Ransom M, Thiel V, et al. Physiologic RNA targets
508 and refined sequence specificity of coronavirus EndoU. RNA. 2020;26(12):1976-99.
509 20. Bhardwaj K, Sun J, Holzenburg A, Guarino LA, Kao CC. RNA recognition and cleavage by
510 the SARS coronavirus endoribonuclease. J Mol Biol. 2006;361(2):243-56.
511 21. Bailey TL, Johnson J, Grant CE, Noble WS. The MEME Suite. Nucleic Acids Res.
512 2015;43(W1):W39-49.
513 22. Will S, Joshi T, Hofacker IL, Stadler PF, Backofen R. LocARNA-P: Accurate boundary
514 prediction and improved detection of structural RNAs. Rna. 2012;18(5):900-14.
515 23. Raden M, Ali SM, Alkhnbashi OS, Busch A, Costa F, Davis JA, et al. Freiburg RNA tools: a
516 central online resource for RNA-focused research and teaching. Nucleic Acids Research.
517 2018;46(W1):W25-W9.
518 24. Hofacker IL. Vienna RNA secondary structure server. Nucleic Acids Res.
519 2003;31(13):3429-31.

520 25. Tavares RCA, Mahadeshwar G, Wan H, Huston NC, Pyle AM. The global and local
521 distribution of RNA structure throughout the SARS-CoV-2 genome. J Virol. 2021;95(5).
522 26. Andrews RJ, O'Leary CA, Tompkins VS, Peterson JM, Haniff HS, Williams C, et al. A map
523 of the SARS-CoV-2 RNA structurome. NAR Genom Bioinform. 2021;3(2):lqab043.
524 27. Gruber AR, Lorenz R, Bernhart SH, Neubock R, Hofacker IL. The Vienna RNA websuite.
525 Nucleic Acids Res. 2008;36(Web Server issue):W70-4.
526 28. Choi R, Zhou M, Shek R, Wilson JW, Tillery L, Craig JK, et al. High-throughput screening of
527 the ReFRAME, Pandemic Box, and COVID Box drug repurposing libraries against SARS-CoV-2
528 nsp15 endoribonuclease to identify small-molecule inhibitors of viral activity. PLoS One.
529 2021;16(4):e0250019.
530 29. Robertson MP, Igel H, Baertsch R, Haussler D, Ares M, Jr., Scott WG. The structure of a
531 rigorously conserved RNA element within the SARS virus genome. PLoS biology. 2005;3(1):e5.
532 30. Tengs T, Kristoffersen AB, Bachvaroff TR, Jonassen CM. A mobile genetic element with
533 unknown function found in distantly related viruses. Virol J. 2013;10:132.
534 31. Frazier MN, Dillard LB, Krahn JM, Perera L, Williams JG, Wilson IM, et al.
535 Characterization of SARS2 Nsp15 nuclease activity reveals it's mad about U. Nucleic Acids Res.
536 2021;49(17):10136-49.
537 32. Patel DK, Gebbie MP, Lee VT. Assessing RNA interactions with proteins by DRaCALA.
538 Methods in enzymology. 2014;549:489-512.
539 33. Orr MW, Lee VT. Differential Radial Capillary Action of Ligand Assay (DRaCALA) for High-
540 Throughput Detection of Protein-Metabolite Interactions in Bacteria. Methods Mol Biol.
541 2017;1535:25-41.
542 34. Bhardwaj K, Palaninathan S, Alcantara JM, Yi LL, Guarino L, Sacchettini JC, et al.
543 Structural and functional analyses of the severe acute respiratory syndrome coronavirus
544 endoribonuclease Nsp15. J Biol Chem. 2008;283(6):3655-64.
545 35. Ricagno S, Egloff MP, Ulferts R, Coutard B, Nurizzo D, Campanacci V, et al. Crystal
546 structure and mechanistic determinants of SARS coronavirus nonstructural protein 15 define an
547 endoribonuclease family. Proc Natl Acad Sci U S A. 2006;103(32):11892-7.
548 36. Xu X, Zhai Y, Sun F, Lou Z, Su D, Xu Y, et al. New antiviral target revealed by the
549 hexameric structure of mouse hepatitis virus nonstructural protein nsp15. J Virol.
550 2006;80(16):7909-17.
551 37. Frazier MN, Wilson IM, Krahn JM, Butay KJ, Dillard LB, Borgnia MJ, et al. Flipped over U:
552 structural basis for dsRNA cleavage by the SARS-CoV-2 endoribonuclease. Nucleic Acids Res.
553 2022.
554 38. Scharpf M, Sticht H, Schweimer K, Boehm M, Hoffmann S, Rosch P. Antitermination in
555 bacteriophage lambda. The structure of the N36 peptide-boxB RNA complex. European journal
556 of biochemistry / FEBS. 2000;267(8):2397-408.
557 39. Legault P, Li J, Mogridge J, Kay LE, Greenblatt J. NMR structure of the bacteriophage
558 lambda N peptide/boxB RNA complex: recognition of a GNRA fold by an arginine-rich motif.
559 Cell. 1998;93(2):289-99.
560 40. Joseph JS, Saikatendu KS, Subramanian V, Neuman BW, Buchmeier MJ, Stevens RC, et al.
561 Crystal structure of a monomeric form of severe acute respiratory syndrome coronavirus
562 endonuclease nsp15 suggests a role for hexamerization as an allosteric switch. J Virol.
563 2007;81(12):6700-8.

564 41. Zhang L, Li L, Yan L, Ming Z, Jia Z, Lou Z, et al. Structural and Biochemical
565 Characterization of Endoribonuclease Nsp15 Encoded by Middle East Respiratory Syndrome
566 Coronavirus. J Virol. 2018;92(22).
567 42. Zheng A, Shi Y, Shen Z, Wang G, Shi J, Xiong Q, et al. Insight into the evolution of
568 nidovirus endoribonuclease based on the finding that nsp15 from porcine Deltacoronavirus
569 functions as a dimer. J Biol Chem. 2018;293(31):12054-67.
570 43. Kim Y, Jedrzejczak R, Maltseva NI, Wilamowski M, Endres M, Godzik A, et al. Crystal
571 structure of Nsp15 endoribonuclease NendoU from SARS-CoV-2. Protein Sci. 2020;29(7):1596-
572 605.
573 44. Pillon MC, Frazier MN, Dillard LB, Williams JG, Kocaman S, Krahn JM, et al. Cryo-EM
574 structures of the SARS-CoV-2 endoribonuclease Nsp15 reveal insight into nuclease specificity
575 and dynamics. Nature communications. 2021;12(1):636.
576 45. Guarino LA, Bhardwaj K, Dong W, Sun J, Holzenburg A, Kao C. Mutational analysis of the
577 SARS virus Nsp15 endoribonuclease: identification of residues affecting hexamer formation. J
578 Mol Biol. 2005;353(5):1106-17.
579 46. Zhao J, Sun L, Zhao Y, Feng D, Cheng J, Zhang G. Coronavirus Endoribonuclease Ensures
580 Efficient Viral Replication and Prevents Protein Kinase R Activation. J Virol. 2020.
581 47. Volk A, Hackbart M, Deng X, Cruz-Pulido Y, O'Brien A, Baker SC. Coronavirus
582 Endoribonuclease and Deubiquitinating Interferon Antagonists Differentially Modulate the Host
583 Response during Replication in Macrophages. J Virol. 2020;94(11).
584 48. Deng X, Buckley AC, Pillatzki A, Lager KM, Faaberg KS, Baker SC. Inactivating Three
585 Interferon Antagonists Attenuates Pathogenesis of an Enteric Coronavirus. J Virol. 2020;94(17).
586 49. Liu X, Fang P, Fang L, Hong Y, Zhu X, Wang D, et al. Porcine deltacoronavirus nsp15
587 antagonizes interferon-beta production independently of its endoribonuclease activity.
588 Molecular immunology. 2019;114:100-7.
589 50. Shokri S, Mahmoudvand S, Taherkhani R, Farshadpour F. Modulation of the immune
590 response by Middle East respiratory syndrome coronavirus. J Cell Physiol. 2019;234(3):2143-51.
591 51. Lei Y, Moore CB, Liesman RM, O'Connor BP, Bergstralh DT, Chen ZJ, et al. MAVS-
592 mediated apoptosis and its inhibition by viral proteins. PLoS One. 2009;4(5):e5466.
593 52. Bhardwaj K, Liu P, Leibowitz JL, Kao CC. The coronavirus endoribonuclease Nsp15
594 interacts with retinoblastoma tumor suppressor protein. J Virol. 2012;86(8):4294-304.
595 53. Athmer J, Fehr AR, Grunewald ME, Qu W, Wheeler DL, Graepel KW, et al. Selective
596 Packaging in Murine Coronavirus Promotes Virulence by Limiting Type I Interferon Responses.
597 mBio. 2018;9(3).
598 54. Wu Y, Zhang H, Shi Z, Chen J, Li M, Shi H, et al. Porcine Epidemic Diarrhea Virus nsp15
599 Antagonizes Interferon Signaling by RNA Degradation of TBK1 and IRF3. Viruses. 2020;12(6).
600 55. Frazier MN, Wilson IM, Krahn JM, Butay KJ, Dillard LB, Borgnia MJ, et al. Flipped over U:
601 structural basis for dsRNA cleavage by the SARS-CoV-2 endoribonuclease. Nucleic Acids Res.
602 2022;50(14):8290-301.
603 56. Stefl R, Allain FH. A novel RNA pentaloop fold involved in targeting ADAR2. RNA.
604 2005;11(5):592-7.
605 57. Perry JK, Appleby TC, Bilello JP, Feng JY, Schmitz U, Campbell EA. An atomistic model of
606 the coronavirus replication-transcription complex as a hexamer assembled around nsp15. J Biol
607 Chem. 2021;297(4):101218.

608 58. Godoy AS, Nakamura AM, Douangamath A, Song Y, Noske GD, Gawriljuk VO, et al.
609 Allosteric regulation and crystallographic fragment screening of SARS-CoV-2 NSP15
610 endoribonuclease. Nucleic Acids Res. 2023.
611 59. Avis JM, Conn GL, Walker SC. Cis-acting ribozymes for the production of RNA in vitro
612 transcripts with defined 5' and 3' ends. Methods Mol Biol. 2012;941:83-98.
613 60. Deng X, Baker SC. An "Old" protein with a new story: Coronavirus endoribonuclease is
614 important for evading host antiviral defenses. Virology. 2018;517:157-63.
615 61. Johnson PZ, Kasprzak WK, Shapiro BA, Simon AE. RNA2Drawer: geometrically strict
616 drawing of nucleic acid structures with graphical structure editing and highlighting of
617 complementary subsequences. RNA Biol. 2019;16(12):1667-71.
618

1A

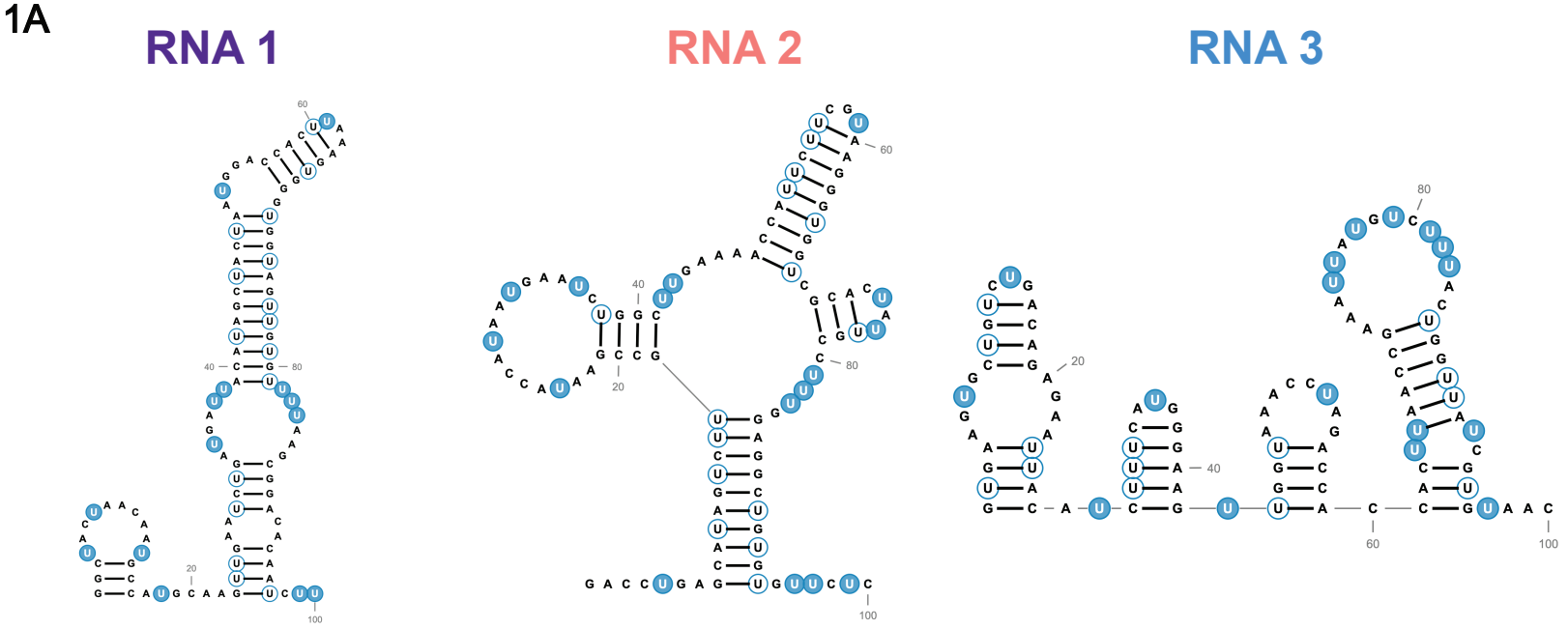

1B

RNA	SARS-CoV-2 gene	Thermodynamic Stability	ΔG of Minimum Free Energy (kcal/mol)	Ensemble Diversity
1	*nsp3*	High	-27.8	4.81
2	*nsp2*	Moderate	-23.4	25.80
3	*nsp13*	Low	-14.2	39.93

1C

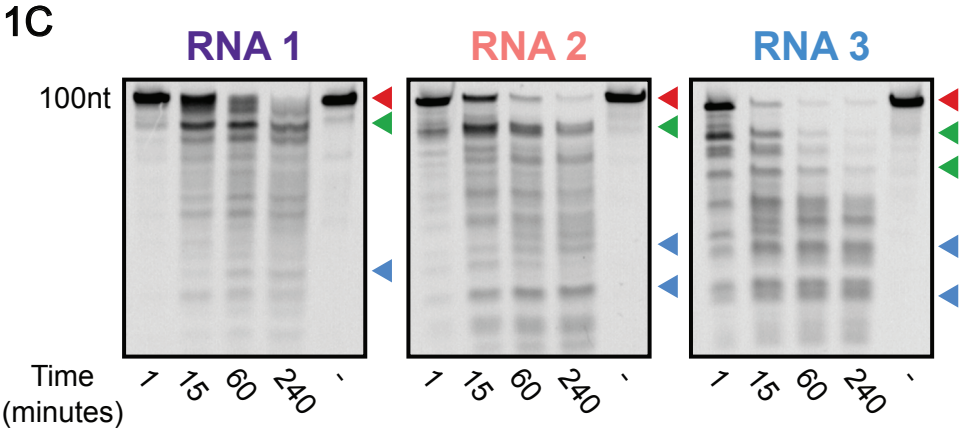

1D

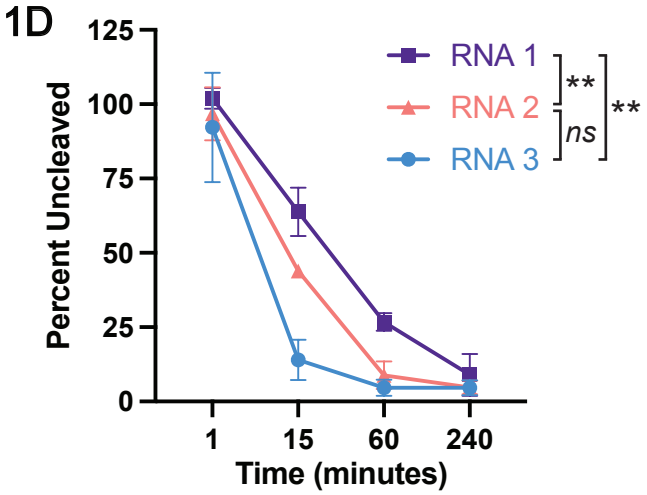

2A

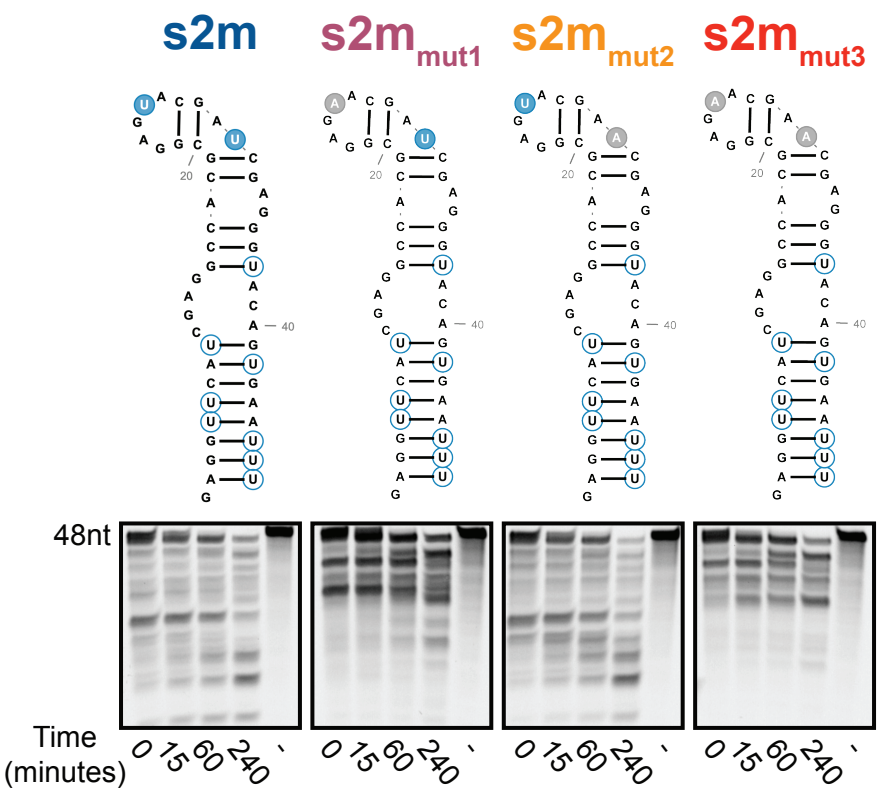

2B

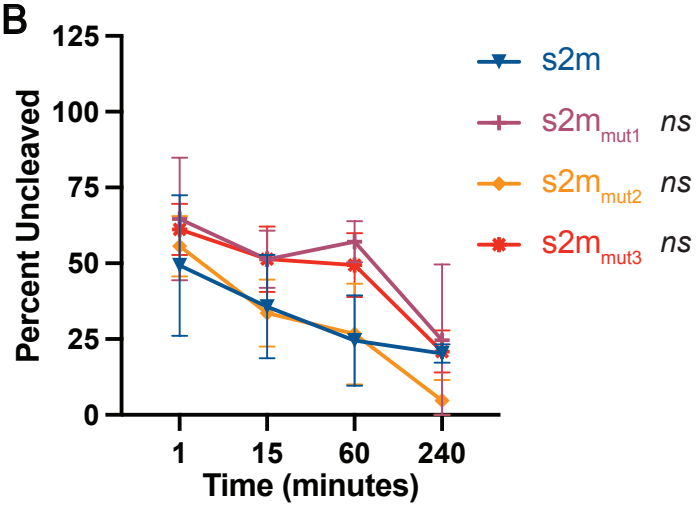

2C

RNA	ΔG of Minimum Free Energy (kcal/mol)	Ensemble Diversity
s2m	-9.4	6.59
$s2m_{mut1}$	-9.4	4.19
$s2m_{mut2}$	-9.4	6.32
$s2m_{mut3}$	-9.4	3.64
Δs2m	-7.9	1.07
$Δs2m_{mut1}$	-7.9	1.07
$Δs2m_{mut2}$	-7.9	1.14
$Δs2m_{mut3}$	-7.9	1.13

2D

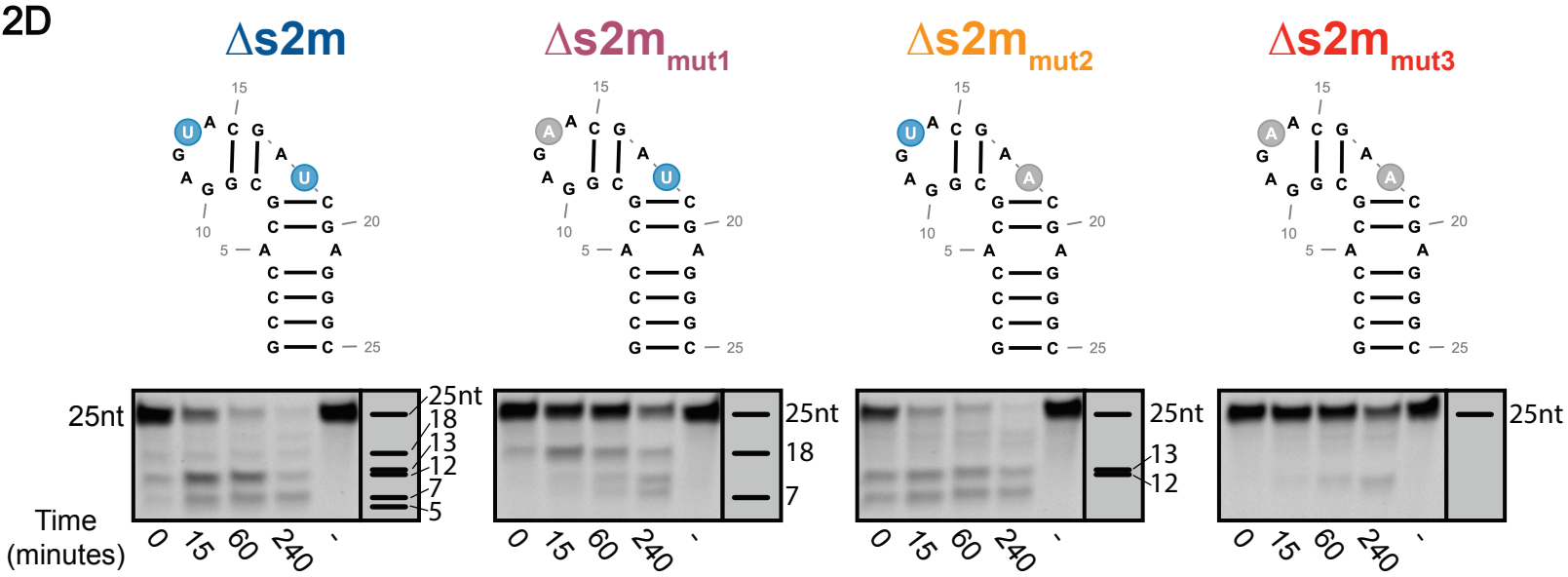

2E

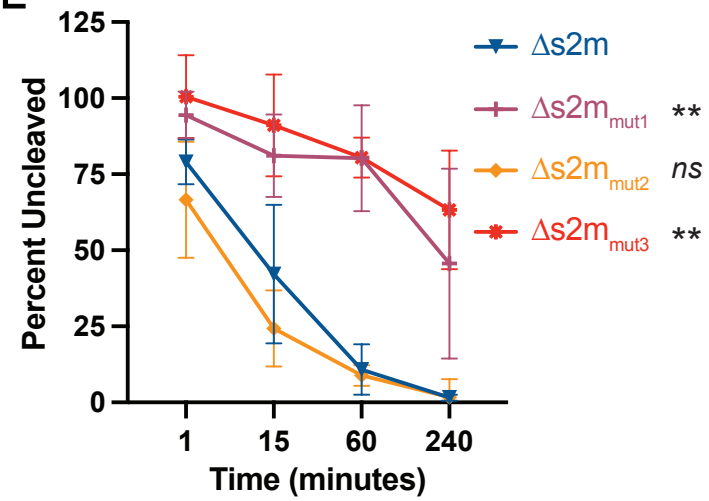

2F

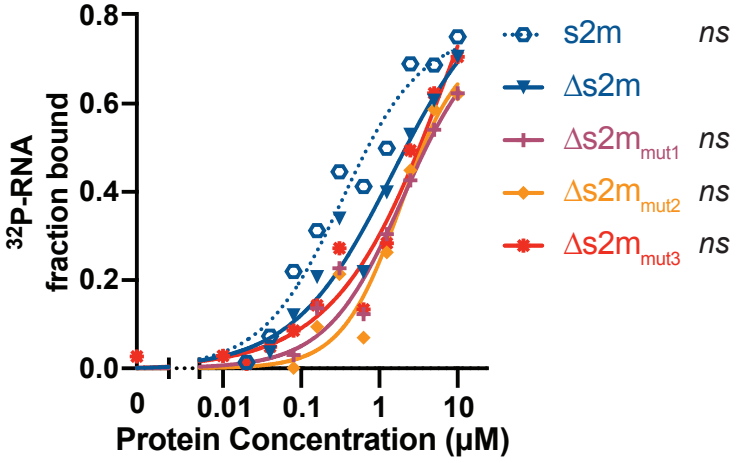

3A

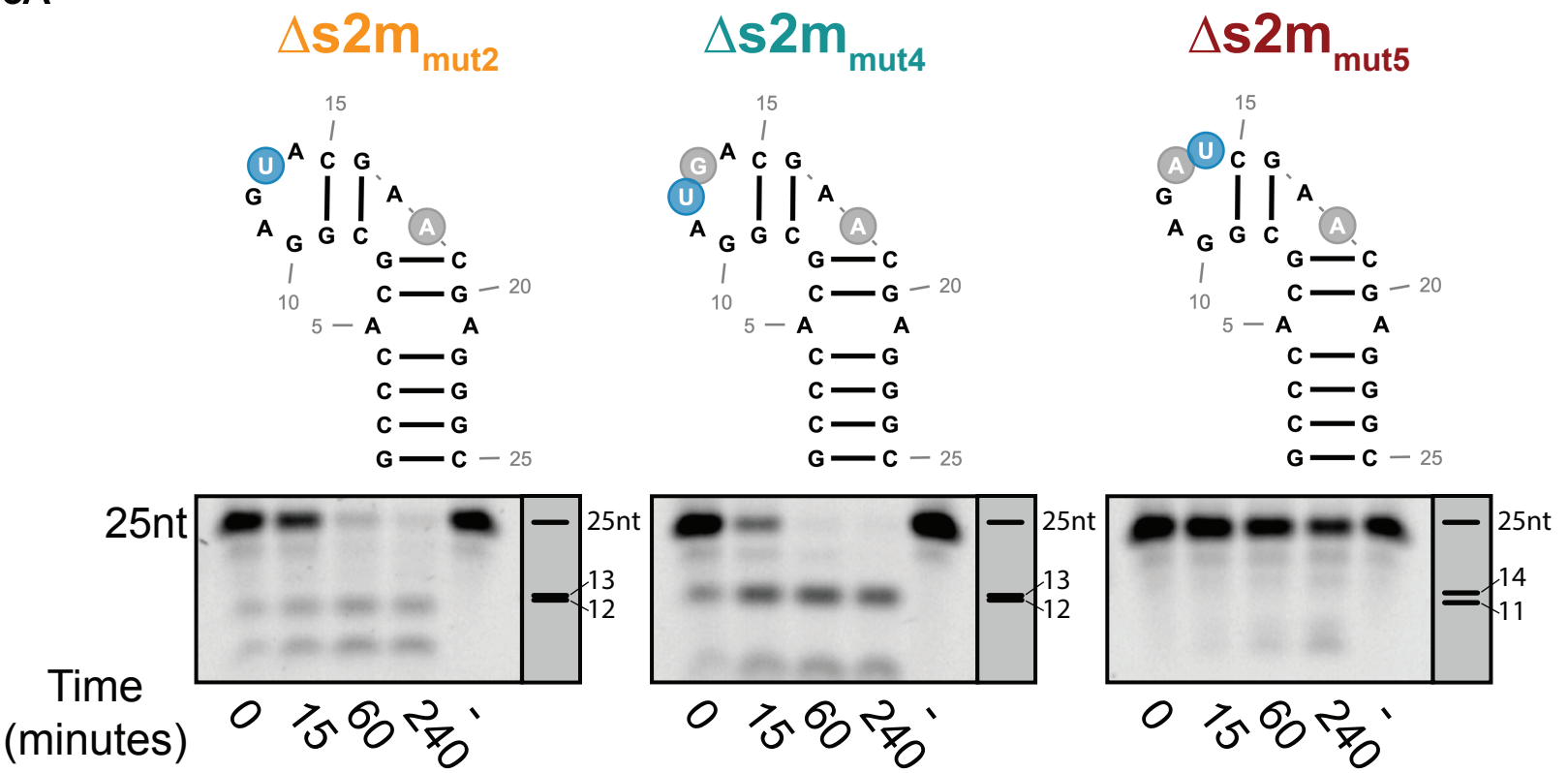

3B

RNA	ΔG of Minimum Free Energy (kcal/mol)	Ensemble Diversity
$\Delta s2m_{mut2}$	-7.9	1.14
$\Delta s2m_{mut4}$	-7.9	1.13
$\Delta s2m_{mut5}$	-6.9	2.32
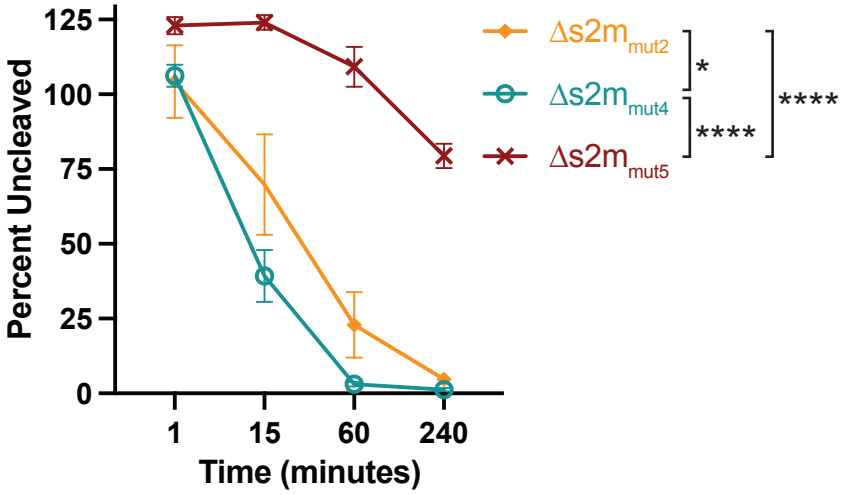
3C